nature immunology

The metabolic ER stress sensor IRE1α suppresses alternative activation of macrophages and impairs energy expenditure in obesity

Bo Shan[1,10], Xiaoxia Wang[1,10], Ying Wu[1,10], Chi Xu[2], Zhixiong Xia[3], Jianli Dai[1], Mengle Shao[4], Feng Zhao[1], Shengqi He[1,5], Liu Yang[6], Mingliang Zhang[6], Fajun Nan[7], Jia Li[7], Jianmiao Liu[3], Jianfeng Liu[3], Weiping Jia[6], Yifu Qiu[8], Baoliang Song[5], Jing-Dong J Han[2], Liangyou Rui[9], Sheng-Zhong Duan[1] & Yong Liu[5]

Obesity is associated with metabolic inflammation and endoplasmic reticulum (ER) stress, both of which promote metabolic disease progression. Adipose tissue macrophages (ATMs) are key players orchestrating metabolic inflammation, and ER stress enhances macrophage activation. However, whether ER stress pathways underlie ATM regulation of energy homeostasis remains unclear. Here, we identified inositol-requiring enzyme 1α (IRE1α) as a critical switch governing M1–M2 macrophage polarization and energy balance. Myeloid-specific IRE1α abrogation in *Ern1*$^{f/f}$; *Lyz2*-Cre mice largely reversed high-fat diet (HFD)-induced M1–M2 imbalance in white adipose tissue (WAT) and blocked HFD-induced obesity, insulin resistance, hyperlipidemia and hepatic steatosis. Brown adipose tissue (BAT) activity, WAT browning and energy expenditure were significantly higher in *Ern1*$^{f/f}$; *Lyz2*-Cre mice. Furthermore, IRE1α ablation augmented M2 polarization of macrophages in a cell-autonomous manner. Thus, IRE1α senses protein unfolding and metabolic and immunological states, and consequently guides ATM polarization. The macrophage IRE1α pathway drives obesity and metabolic syndrome through impairing BAT activity and WAT browning.

Obesity is associated with a state of chronic low-grade inflammation characterized by infiltration and activation of immune cells in metabolic organs such as adipose tissue[1,2]. Overnutrition-induced metabolic inflammation in adipose tissue has been proposed to be critical in the pathogenesis of insulin resistance and type 2 diabetes[3]. Adipose tissue is composed of multiple types of tissue, including white, brown and beige fat, which play pivotal roles in metabolic homeostasis[4]. Various innate and adaptive immune cells communicate with adipocytes and thereby maintain adipose function[5]. In particular, ATMs are critical in orchestrating metabolic inflammation[6–10]. As the major effector cells mediating both adipose and systemic inflammation, ATMs respond to metabolic cues and are present in a spectrum of functionally distinct activation states, thereby exerting profound regulatory effects on metabolism[6,8–11]. In obesity, ATMs have been found in the so-called 'crown-like' structure (CLS) around dying adipocytes, which display a predominantly proinflammatory classically activated (M1) phenotype[1]. ATM M1 polarization is thought to promote insulin resistance and type 2 diabetes[1,6,9,10]. Whereas in the lean state, ATMs are uniformly dispersed, primarily exhibiting an anti-inflammatory alternatively activated (M2) phenotype[1,7,12]. ATM M2 polarization, induced by eosinophil-derived type 2 cytokines (for example, the interleukins IL-4 and IL-13), enhances activation of BAT and browning or beiging of WAT[13–15], thereby modulating adaptive thermogenesis and energy expenditure.

The ER is a critical organelle in cellular nutrient sensing and handling[2]. An overload of protein folding can trigger ER stress and consequently activate the unfolded protein response (UPR). Three UPR pathways coordinately restore ER homeostasis and affect many aspects of cellular function[16–18]. IRE1, the ER-resident transmembrane protein kinase and endoribonuclease, is the most conserved ER stress sensor[18,19]. Mammalian IRE1α is activated by ER stress and consequently can catalyze the unconventional splicing of the mRNA encoding the transcription factor X-box binding protein 1 (XBP1) or can degrade select mRNA species in a process termed regulated IRE1-dependent decay (RIDD)[18,19]. Hyperactivation of the IRE1α–XBP1 pathway has been documented in the adipose

[1]Key Laboratory of Nutrition and Metabolism, Institute for Nutritional Sciences, Shanghai Institutes for Biological Sciences, Chinese Academy of Sciences, University of the Chinese Academy of Sciences, Shanghai, China. [2]Key Laboratory of Computational Biology, Chinese Academy of Sciences–Max Planck Partner Institute for Computational Biology, Shanghai Institutes for Biological Sciences, Chinese Academy of Sciences, Shanghai, China. [3]Cellular Signaling Laboratory, Key Laboratory of Molecular Biophysics of the Ministry of Education, Huazhong University of Science and Technology, Wuhan, China. [4]Touchstone Diabetes Center, Department of Internal Medicine, University of Texas Southwestern Medical Center, Dallas, Texas, USA. [5]Hubei Key Laboratory of Cell Homeostasis, College of Life Sciences, Institute for Advanced Studies, Wuhan University, Wuhan, China. [6]Shanghai Diabetes Institute, Shanghai Key Laboratory of Diabetes Mellitus, Shanghai Clinical Center for Diabetes, Department of Endocrinology and Metabolism, Shanghai Jiao Tong University Affiliated Sixth People's Hospital, Shanghai, China. [7]National Center for Drug Screening, Shanghai Institute of Materia Medica, Chinese Academy of Sciences, Shanghai, China. [8]Institute of Molecular Medicine, Peking-Tsinghua Center for Life Sciences, Academy for Advanced Interdisciplinary Studies, Beijing Key Laboratory of Cardiometabolic Molecular Medicine, Peking University, Beijing, China. [9]Department of Molecular and Integrative Physiology, University of Michigan Medical School, Ann Arbor, Michigan, USA. [10]These authors contributed equally to this work. Correspondence should be addressed to S.Z.D. (szduan@sibs.ac.cn) or Y.L. (liuyong31279@whu.edu.cn or liuy@sibs.ac.cn).

Received 9 January; accepted 13 February; published online 27 March 2017; doi:10.1038/ni.3709

tissue of obese humans[20,21], but whether this hyperactivation is causally related to energy imbalance remains unknown. Here, we sought to test the possibility that during chronic handling of excess nutrients, ER stress mechanistically converges with metabolic inflammation through ATMs, thereby initiating adipose dysfunction and causing dysregulation of glucose and energy metabolism. We found that the IRE1α pathway in macrophages regulates a shift in M1–M2 polarization and couples metabolic ER stress to the disruption of energy balance through impairing BAT activity and WAT browning.

RESULTS

Myeloid IRE1α ablation prevents diet-induced obesity

We first examined whether ER stress in ATMs accompanies overnutrition-induced obesity and metabolic inflammation in adipose tissue, such as in visceral epididymal WAT (epWAT) of obese mice fed an HFD (**Supplementary Fig. 1a**,**b**). Not only in adipocytes but also in the stromal vascular fraction (SVF), where resident ATMs are enriched[1], we observed significantly elevated *Xbp1* mRNA splicing and higher expression levels of the UPR marker and proinflammatory genes (**Supplementary Fig. 1c**–**f**). Moreover, in cells positive for the integrin CD11b (CD11b$^+$), which were isolated from SVFs of obese mice and largely comprised macrophages, we also detected prominently increased *Xbp1* mRNA splicing and decreased mRNA abundance of two known RIDD-target genes[22], *Hgsnat* and *Pmp22*, along with elevated expression of other UPR markers and proinflammatory genes (**Supplementary Fig. 1g**,**h**). This finding suggested that excessive nutrient handling elicits metabolic ER stress and activation of the IRE1α branch of the UPR in ATMs in parallel with adipose inflammation. To investigate whether the IRE1α pathway in macrophages exerts metabolic actions during overnutrition, we intercrossed floxed IRE1α (*Ern1*$^{f/f}$) mice[23] with the Lysozyme 2-Cre (*Lyz2*-Cre) line[13] to create myeloid-specific IRE1α-knockout (*Ern1*$^{f/f}$; *Lyz2*-Cre) mice, in which IRE1α protein expression was abolished in bone-marrow-derived macrophages (BMDMs) and peritoneal macrophages (pMϕ) but remained normal in epWAT and subcutaneous WAT (scWAT) (**Fig. 1a**) as well as in other tissues examined (**Supplementary Fig. 2a**). RT–PCR analysis with primers spanning the 121-bp exon 2 of *Ern1* that was targeted for deletion revealed that IRE1α was efficiently ablated in BMDMs and pMϕ, and was partially ablated in neutrophils but not in T cells positive for the monomorphic co-receptor CD4 (CD4$^+$) or B cells (**Fig. 1b**). In comparison to their *Ern1*$^{f/f}$ counterparts, *Ern1*$^{f/f}$; *Lyz2*-Cre mice showed no defective developmental phenotypes (**Supplementary Fig. 2b**,**c**) and had insignificant differences in body weight but lower body fat mass when they were fed a normal chow (NC) diet (**Fig. 1c**,**d** and **Supplementary Fig. 2d**). Remarkably, these mice were completely resistant to HFD-induced obesity, exhibiting much lower body weight and adiposity without significant changes in their lean mass (**Fig. 1c**,**d** and **Supplementary Fig. 2b**,**e**–**g**). *Ern1*$^{f/f}$; *Lyz2*-Cre mice after HFD feeding also displayed a more beneficial epWAT phenotype with smaller adipocytes (**Fig. 1e**), along with significantly decreased hyperleptinemia and normal serum adiponectin levels (**Fig. 1f**), thus indicating improved adipose function. Moreover, HFD-fed *Ern1*$^{f/f}$; *Lyz2*-Cre mice showed greatly decreased hyperinsulinemia (**Fig. 1g**) and markedly improved insulin sensitivity (**Supplementary Fig. 2h**) and blood glucose control (**Fig. 1h**). In addition, *Ern1*$^{f/f}$; *Lyz2*-Cre mice did not exhibit HFD-induced hypertriglyceridemia, hypercholesterolemia or hepatosteatosis (**Fig. 1i**–**k** and **Supplementary Fig. 2i**). These data demonstrated that IRE1α in myeloid cells couples overnutrition to the development of obesity and obesity-associated metabolic deterioration.

Myeloid IRE1α abrogation increases energy expenditure

We next determined whether myeloid IRE1α deficiency affects energy balance. *Ern1*$^{f/f}$; *Lyz2*-Cre mice and their *Ern1*$^{f/f}$ counterparts had similar daily food consumption during NC or HFD feeding (**Supplementary Fig. 2j**) and showed comparable absorption of dietary lipids when they were maintained on an HFD (**Supplementary Fig. 2k**). However, oxygen consumption, when normalized to the lean mass, was significantly higher in *Ern1*$^{f/f}$; *Lyz2*-Cre mice than in *Ern1*$^{f/f}$ littermates fed either NC or an HFD (**Fig. 2a**,**b**), although physical activities were similar between these two groups (**Supplementary Fig. 2l**). In addition, core body temperatures were also higher in HFD-fed *Ern1*$^{f/f}$; *Lyz2*-Cre mice (**Fig. 2c**). Thus, loss of IRE1α in myeloid cells resulted in increased energy expenditure.

To determine whether the effect of myeloid IRE1α deficiency on energy expenditure might be attributable to enhanced heat production, we first examined the activation of BAT, the major organ that dissipates energy through the action of mitochondrial uncoupling protein 1 (UCP1) during adaptive thermogenesis[4,24]. In the BAT of HFD-fed *Ern1*$^{f/f}$; *Lyz2*-Cre mice, compared with their *Ern1*$^{f/f}$ counterparts, much lower lipid-droplet content (**Fig. 2d**) and higher expression of UCP1 protein were observed (**Fig. 2e**). *Ern1*$^{f/f}$; *Lyz2*-Cre mice fed either NC or an HFD had significantly elevated expression of key thermogenic genes in BAT, thus further suggesting that these mice had a greater BAT thermogenic capacity (**Fig. 2f**). In parallel with higher levels of UCP1 protein, BAT from HFD-fed *Ern1*$^{f/f}$; *Lyz2*-Cre mice also had increased levels of phosphorylated STAT3 (p-STAT3) transcription factor and elevated expression of tyrosine hydroxylase (TH) (**Fig. 2g**), the rate-limiting enzyme in biosynthesis of catecholamines, which activate both brown and beige fat, thereby generating heat[13,14]. Given the critical function of the inducible beige fat within scWAT in adaptive thermogenesis and maintenance of energy balance[4,24], we examined whether beige adipocytes were also involved. Indeed, scWAT from HFD-fed *Ern1*$^{f/f}$; *Lyz2*-Cre animals exhibited significantly elevated *Ucp1* mRNA and UCP1 protein expression levels (**Fig. 2h**,**i**), thus indicating enhanced beige-fat activation.

To confirm the effect of myeloid IRE1α abrogation on adaptive thermogenesis, we subjected mice to cold stress (4 °C). *Ern1*$^{f/f}$; *Lyz2*-Cre mice maintained their body temperatures at higher levels than *Ern1*$^{f/f}$ animals after cold exposure for 3 d (**Fig. 3a**) but showed no significant changes in BAT weight (**Fig. 3b**). However, cold stress decreased BAT lipid-droplet levels (**Fig. 3c**) and increased BAT UCP1 and TH expression (**Fig. 3d**,**e**) as well as norepinephrine content (**Fig. 3f**) to a greater extent in *Ern1*$^{f/f}$; *Lyz2*-Cre mice, thus indicating higher BAT activity accompanied by augmented biosynthesis of catecholamines. In addition, scWAT of *Ern1*$^{f/f}$; *Lyz2*-Cre mice subjected to cold exposure also exhibited markedly enhanced remodeling, as evidenced by both increased induction of multilocular UCP1-expressing beige adipocytes (**Fig. 3g**,**h**) and robust augmentation of cold-induced UCP1 expression and norepinephrine production (**Fig. 3i**,**j**). Together, these results demonstrated that the loss of myeloid IRE1α promotes energy expenditure through enhancing the thermogenic activity of both brown and beige fat.

To determine whether the effect of myeloid IRE1α deficiency on adaptive thermogenesis stems primarily from its actions in ATMs, we used liposomal clodronate, which selectively depletes macrophages but not neutrophils through induction of apoptosis[25], even in the WAT of obese mice[26]. Indeed, administration of clodronate-containing liposomes into the scWAT of *Ern1*$^{f/f}$ or *Ern1*$^{f/f}$; *Lyz2*-Cre mice resulted in marked decreases in the mRNA expression of the macrophage marker F4/80 (encoded by *Adgre1*) (**Fig. 4a**), thus indicating efficient ablation of ATMs in scWAT in both groups. Clodronate

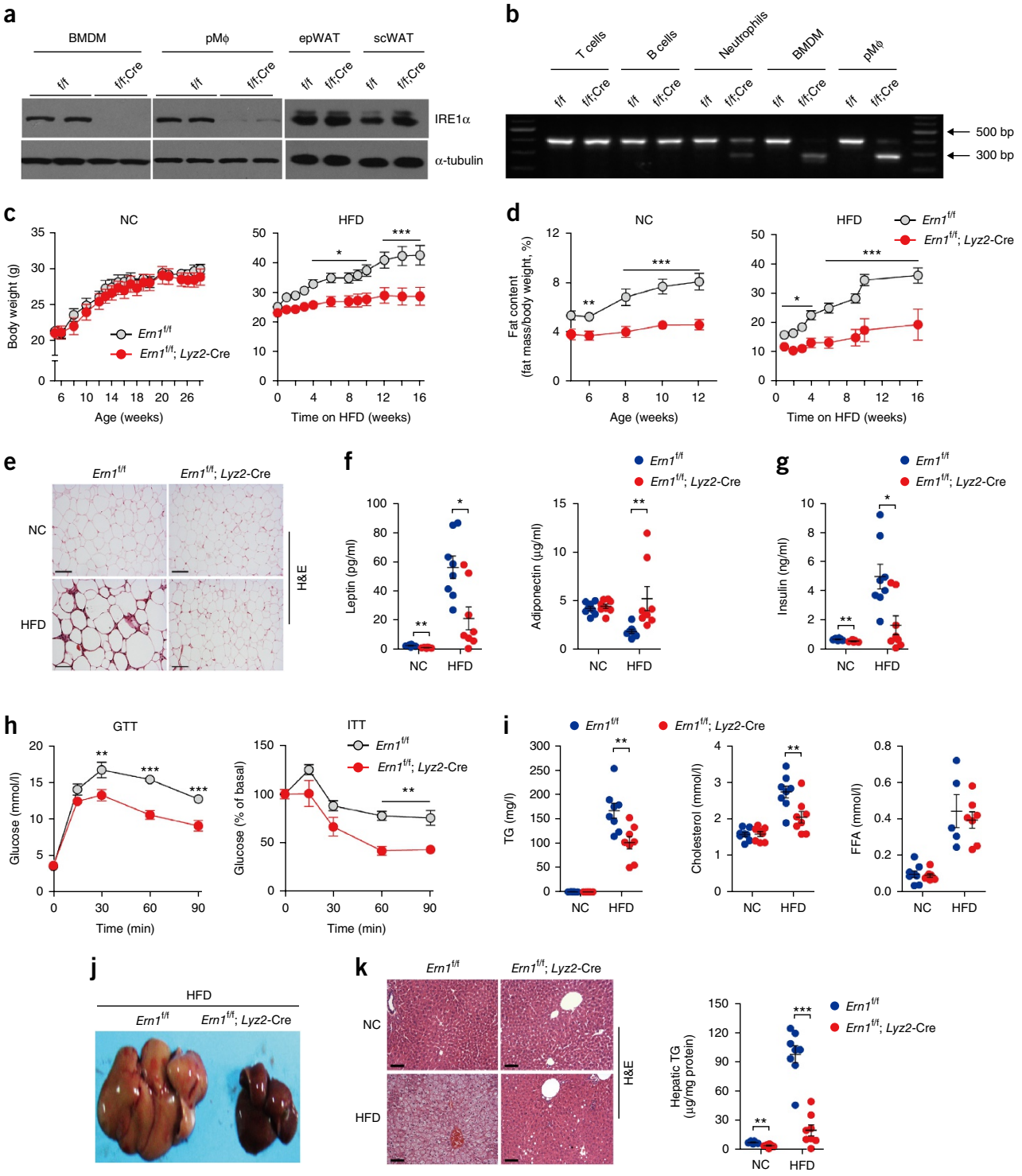

Figure 1 Myeloid IRE1α abrogation protects mice from diet-induced obesity and metabolic syndrome. (**a**) Immunoblot analyses of IRE1α protein in bone-marrow-derived macrophages (BMDM), peritoneal macrophages (pMϕ) and epididymal (ep) and subcutaneous (sc) WAT from male *Ern1*$^{f/f}$; *Lyz2*-Cre (f/f;Cre) mice and *Ern1*$^{f/f}$ (f/f) littermates. α-tubulin is a loading control. (**b**) RT–PCR analyses of the region spanning the targeted exon 2 within *Ern1* mRNA in CD4$^+$ T cells, B cells and neutrophils from the spleen, as well as in BMDMs and pMϕ. (**c**–**k**) Male *Ern1*$^{f/f}$; *Lyz2*-Cre mice and age-matched *Ern1*$^{f/f}$ littermates were fed a normal chow diet (NC, 10% fat; $n = 8$ per group) or a high-fat diet (HFD, 60% fat; $n = 10$ per group). HFD feeding started at 8 weeks of age. (**c**) Body weight. (**d**) Body-fat content. (**e**–**k**) Metabolic measurements in mice after feeding of an NC or HFD for 16 weeks ($n = 8$ per group). (**e**) Hematoxylin and eosin (H&E) staining of epWAT sections (four images per mouse). Scale bars, 10 μm. (**f**) Serum concentrations of leptin and adiponectin. (**g**) Serum insulin levels. (**h**) Glucose tolerance test (GTT) and insulin tolerance test (ITT). (**i**) Serum levels of triglycerides (TG), cholesterol and free fatty acids (FFA). (**j**) Representative images of livers from HFD-fed mice (3 images per mouse). (**k**) Representative images of H&E staining of liver sections (4 images per mouse). Scale bars, 200 μm. Hepatic TG content was determined. All data are shown as mean ± s.e.m., $^*P < 0.05$; $^{**}P < 0.01$; $^{***}P < 0.001$ by two-tailed Student's *t* test or two-way ANOVA.

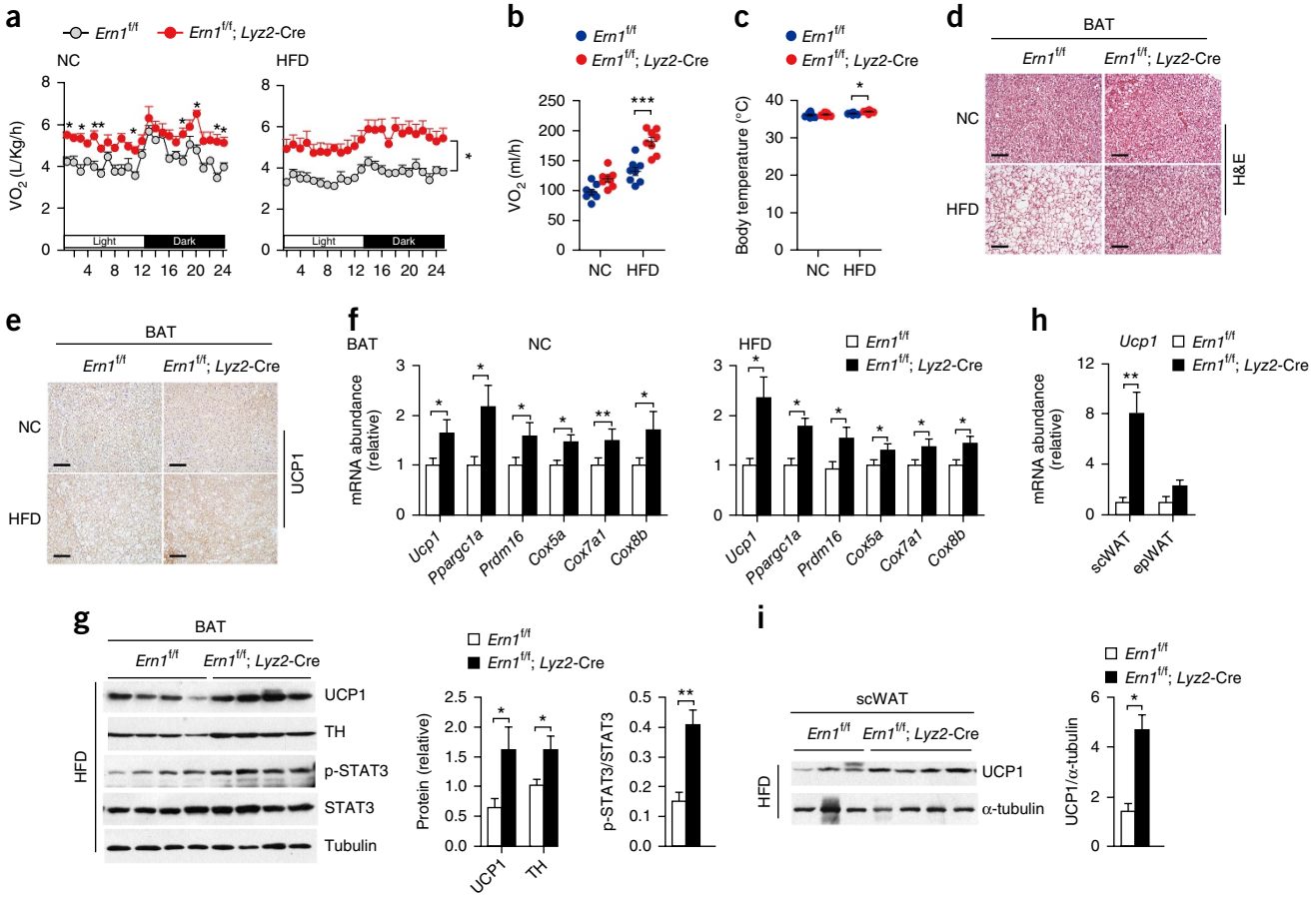

Figure 2 Myeloid IRE1α ablation increases energy expenditure via enhancing brown- and beige-fat activation. Male *Ern1*$^{f/f}$; *Lyz2*-Cre and *Ern1*$^{f/f}$ mice were fed an NC or HFD for 16 weeks ($n = 8$ per group). (**a**,**b**) Oxygen consumption (VO_2) monitored over a 24-h period (**a**) and shown as averaged values (**b**). (**c**) Core body temperatures of mice housed at 22 °C. (**d**,**e**) Representative images of H&E staining (**d**) and UCP1 immunohistochemistry (IHC) (**e**) of BAT sections (5 images per mouse). Scale bars, 200 μm. (**f**) Quantitative RT–PCR analysis of the mRNA abundance of the indicated thermogenic genes in BAT. (**g**) Immunoblot analysis and quantification of UCP1 and tyrosine hydroxylase (TH) protein and STAT3 phosphorylation in BAT from HFD-fed mice. α-tubulin is a loading control. (**h**) Quantitative RT–PCR analysis of the mRNA abundance of *Ucp1* in scWAT and epWAT of mice after HFD feeding. (**i**) Immunoblot analysis and quantification of UCP1 protein in scWAT of HFD-fed mice. Results are presented as mean ± s.e.m., $^*P < 0.05$; $^{**}P < 0.01$ by two-tailed Student's *t* test or two-way ANOVA.

treatment impaired the enhancement of scWAT remodeling (**Fig. 4b**) and greatly diminished the UCP1 induction in *Ern1*$^{f/f}$; *Lyz2*-Cre mice after cold exposure (**Fig. 4c**,**d**). Hence, these results clearly demonstrated the critical role of IRE1α-deficient ATMs in promoting WAT browning during adaptive thermogenesis.

IRE1α deficiency reverses the M1–M2 imbalance of ATMs

We then considered whether macrophage IRE1α might be coupled to metabolic inflammation by mediating a shift in M1–M2 polarization of ATMs. As compared with their *Ern1*$^{f/f}$ counterparts, HFD-fed *Ern1*$^{f/f}$; *Lyz2*-Cre mice exhibited significantly decreased serum levels of proinflammatory cytokines such as tumor necrosis factor (TNF), IL-1β and the chemokine CCL2 (**Fig. 5a**); however, they produced higher amounts of IL-6 (**Fig. 5a**), a pleiotropic cytokine that exerts either proinflammatory or anti-inflammatory effects. Immunohistochemistry also revealed lower numbers of epWAT F4/80$^+$ CLS in *Ern1*$^{f/f}$; *Lyz2*-Cre than in *Ern1*$^{f/f}$ mice after HFD feeding (**Fig. 5b**). The CD11b$^+$F4/80$^+$ cell numbers in epWAT and scWAT SVFs, as measured by flow cytometry, were ~58% and ~26% lower, respectively, in HFD-fed *Ern1*$^{f/f}$; *Lyz2*-Cre mice (**Fig. 5c**,**d**), thus indicating dramatically decreased macrophage recruitment in WAT. We detected an ~39% decrease in M1-like CD11b$^+$CD11c$^+$ cells and an ~161% increase in M2-like CD11b$^+$CD206$^+$ cells in both epWAT (**Fig. 5e**,**f**) and scWAT SVFs (**Fig. 5g**,**h**). Notably, in the setting of NC feeding, SVFs of epWAT from *Ern1*$^{f/f}$; *Lyz2*-Cre mice, compared with their *Ern1*$^{f/f}$ counterparts, had comparable amounts of CD11b$^+$F4/80$^+$ cells but considerably increased CD11b$^+$CD206$^+$ cells (**Supplementary Fig. 3a**,**b**). These results suggest that in the absence of excess nutrition, IRE1α ablation does not influence macrophage differentiation or recruitment. Moreover, in SVFs of both epWAT (**Fig. 5i**) and scWAT (**Fig. 5j**) of HFD-fed *Ern1*$^{f/f}$; *Lyz2*-Cre mice, gene expression profiling showed robust increases in the expression of signature M2-marker genes (*Arg1*, *Chil3*, *Retnla*, *Mrc1*, *Pdcd1lg2* and *Il10*)[7,12] and significant decreases in the expression of M1 markers (*Nos2*, *Il6* and *Tnf*)[1]. Additionally, in SVFs of BAT from *Ern1*$^{f/f}$; *Lyz2*-Cre mice after HFD feeding, M2- but not M1-marker genes were also similarly upregulated (**Fig. 5k**). In agreement with their serum levels (**Fig. 5a**), the expression of proinflammatory adipokines *Tnf*, *Ccl2* and *Il1b* markedly decreased, whereas that of *Il6* dramatically increased in adipocytes of both epWAT and scWAT (**Fig. 5i**,**j**). Next, we examined whether myeloid IRE1α deficiency blunted HFD-induced adipose inflammation through altering the UPR pathways. In *Ern1*$^{f/f}$; *Lyz2*-Cre mice subjected to HFD feeding, there were no significant changes in the expression of typical ER stress markers, including *Bip*

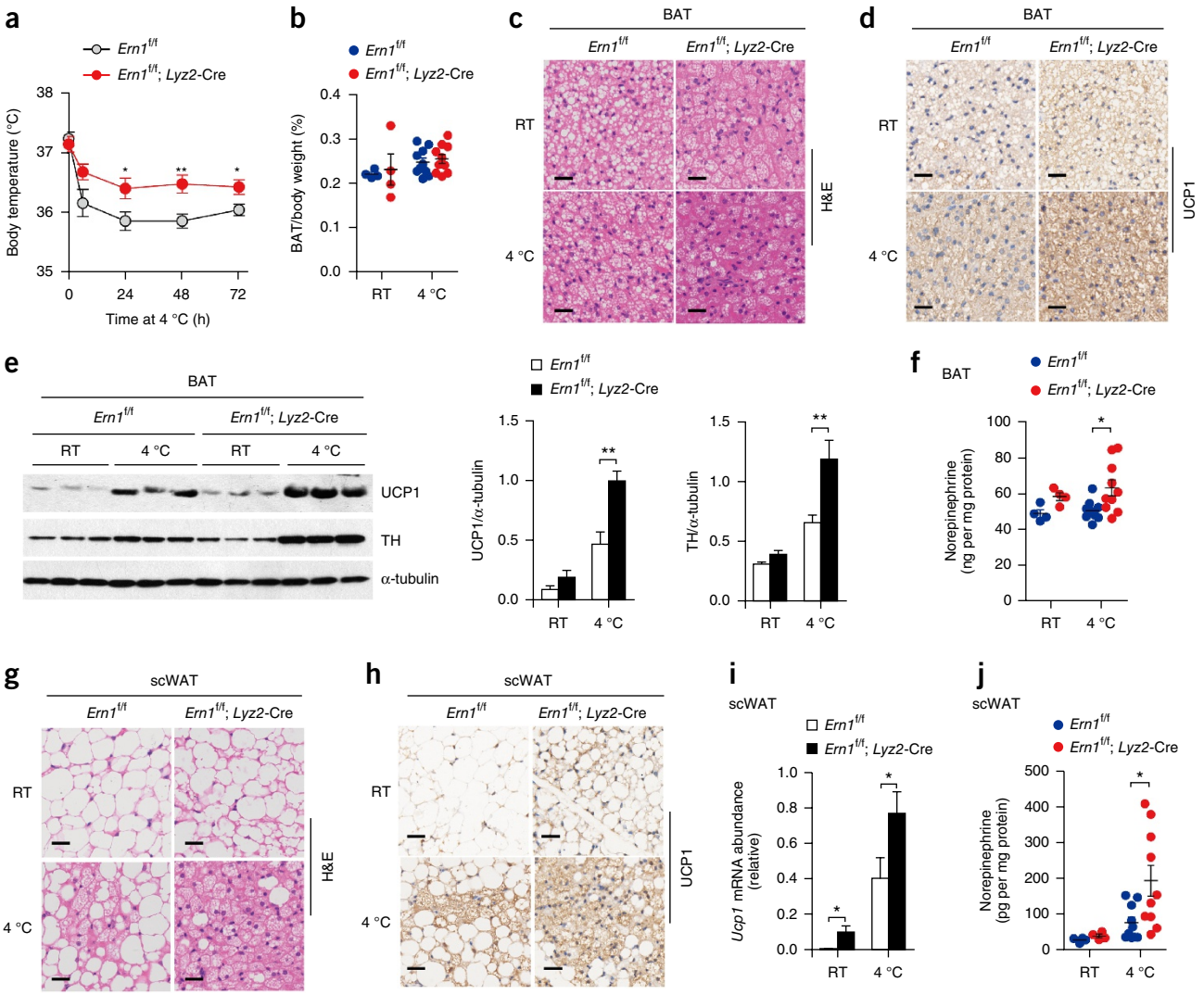

Figure 3 Myeloid IRE1α ablation augments adaptive thermogenesis. NC-fed *Ern1*$^{f/f}$; *Lyz2*-Cre and *Ern1*$^{f/f}$ mice were maintained at room temperature (RT, ~26 °C; $n = 4$ per group) or at 4 °C for 72 h ($n = 10$ per group). (**a**) Core body temperatures of mice maintained at 4 °C. (**b**) Relative BAT weight after exposure to room temperature or cold stress. (**c**,**d**) Representative images of H&E staining (**c**) and UCP1 IHC (**d**) of BAT sections (6 images per mouse). Scale bars, 30 μm. (**e**) Immunoblot analysis and quantification of BAT UCP1 and TH protein. α-tubulin is a loading control. (**f**) BAT norepinephrine content, as measured by enzyme-linked immunosorbent assay. (**g**,**h**) Representative images of H&E staining (**g**) and UCP1 IHC (**h**) of scWAT sections (6 images per mouse). Scale bars, 30 μm. (**i**) Relative mRNA abundance of *Ucp1* in scWAT. (**j**) Norepinephrine content in scWAT. Results are presented as mean ± s.e.m., $*P < 0.05$; $**P < 0.01$ by two-tailed Student's *t* test or two-way ANOVA.

(official symbol *Hspa5*), *Chop* (official symbol *Ddit3*) and *Atf4*, in the SVFs or adipocytes of epWAT or scWAT (**Supplementary Fig. 3c–f**). Further, in CD11b$^+$ cells isolated from SVFs, which predominantly consisted of CD11b$^+$F4/80$^+$ ATMs (>82% in epWAT, >73% in scWAT; **Supplementary Fig. 4**), elevated levels of the M2-marker protein Ym-1 (encoded by *Chil3*) were detected in HFD-fed *Ern1*$^{f/f}$; *Lyz2*-Cre mice as compared with their *Ern1*$^{f/f}$ counterparts (**Fig. 5l**,**m**). No apparent alterations in phosphorylation of the initiation factor eIF2α or levels of the prosurvival ER chaperone BiP and the heat-shock protein Hsp90 were observed in isolated CD11b$^+$ cells or adipocytes (**Fig. 5l**,**m**). Together, these data suggested that macrophage IRE1α ablation can unlock its suppressive action in M2 polarization of ATMs, thereby reversing HFD-induced M1–M2 imbalance in WAT, decreasing adipose inflammation and enhancing energy expenditure. Without affecting the ER stress state in adipose tissue, loss of IRE1α in ATMs can resolve overnutrition-induced metabolic inflammation.

IRE1α promotes M2 polarization in a cell-autonomous manner

To determine whether IRE1α regulates macrophage polarization in a cell-autonomous fashion, we used lipopolysaccharide (LPS) and IL-4 stimulation of mouse BMDM *in vitro* models to mimic M1 and M2 polarization[27], respectively. As assessed with an antibody to IRE1α phosphorylated at Ser724 within the activation loop of its kinase domain[28], LPS treatment increased IRE1α phosphorylation in BMDMs (**Fig. 6a**); however, phos-tag gel analysis[29] indicated that LPS-stimulated IRE1α phosphorylation was distinct from that induced by the typical ER stressor thapsigargin (**Supplementary Fig. 5a**). In addition, LPS did not affect eIF2α phosphorylation or BiP protein expression (**Fig. 6a** and **Supplementary Fig. 5b**). This result is consistent with the previously reported finding that Toll-like-receptor ligands such as LPS specifically activate the IRE1α pathway in macrophages[30]. In *Ern1*$^{f/f}$; *Lyz2*-Cre BMDMs, compared with control *Ern1*$^{f/f}$ BMDMs, LPS induction of inducible nitric oxide synthase (iNOS)

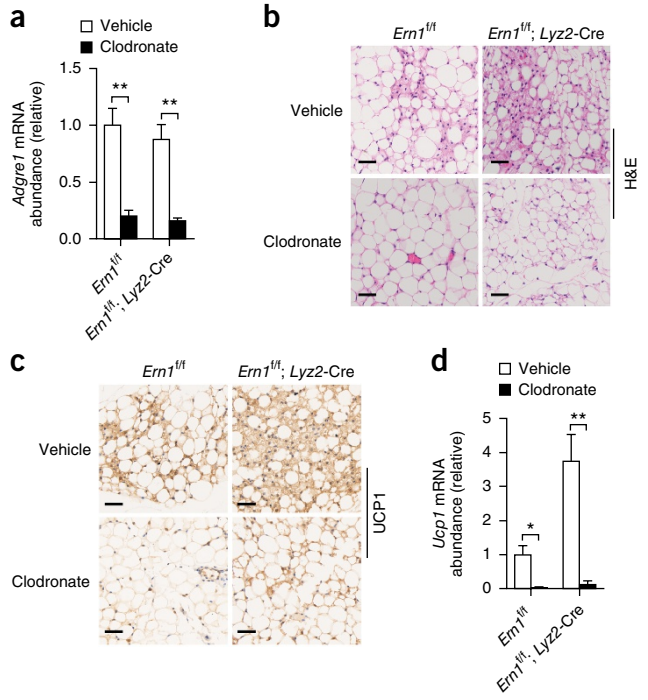

Figure 4 Depletion of ATMs abolishes cold-induced scWAT browning. Clodronate liposomes or control liposomes (vehicle) were subcutaneously delivered into scWAT of NC-fed *Ern1*$^{f/f}$; *Lyz2*-Cre and *Ern1*$^{f/f}$ mice. Animals were subsequently maintained at 4 °C for 72 h ($n = 6$ per group). (**a**) Relative mRNA abundance of *Adgre1* in scWAT. (**b**,**c**) Representative images of H&E staining (**b**) and UCP1 IHC (**c**) of scWAT sections (6 images per mouse). Scale bars, 30 μm. (**d**) Relative mRNA abundance of *Ucp1* in scWAT. Data are shown as mean ± s.e.m., $*P < 0.05$; $**P < 0.01$ by two-way ANOVA.

protein expression was significantly lower (**Fig. 6a**). Flow cytometry analysis showed an ~34% decrease in F4/80$^+$CD11c$^+$ cell number from LPS-treated *Ern1*$^{f/f}$; *Lyz2*-Cre BMDMs (**Fig. 6b**). LPS-induced upregulation of *Il6* mRNA was also significantly decreased in *Ern1*$^{f/f}$; *Lyz2*-Cre cells (**Fig. 6c**), in agreement with results from previous studies showing that IRE1α increases the expression of proinflammatory cytokines in macrophages[30,31]. IL-4 also stimulated IRE1α phosphorylation, as detected by the antibody to phospho-IRE1α or by phos-tag gel analysis (**Fig. 6d** and **Supplementary Fig. 5c**). By contrast, IL-4 treatment had no stimulatory effect on eIF2α phosphorylation or BiP protein abundance (**Fig. 6d** and **Supplementary Fig. 5d**), thus suggesting that IL-4 also selectively activates the IRE1α branch. In *Ern1*$^{f/f}$; *Lyz2*-Cre BMDMs, compared with *Ern1*$^{f/f}$ BMDMs, IL-4 stimulation of Ym-1 protein was significantly elevated, but there were no changes in phosphorylation of the transcription factor STAT6 (**Fig. 6d**). Furthermore, IL-4-treated *Ern1*$^{f/f}$; *Lyz2*-Cre BMDMs had an ~46% increase in CD11b$^+$CD206$^+$ cells (**Fig. 6e**) and showed robustly enhanced expression of signature M2-marker genes (**Fig. 6f**). These results demonstrated that loss of IRE1α was sufficient to promote IL-4 induction of M2 polarization while dampening LPS stimulation of M1 polarization.

We then sought to assess metabolic cross-talk between M2-polarized macrophages and beige adipocytes, and to determine whether such cross-talk might be influenced by IRE1α ablation in macrophages. We used UCP1-expressing beige adipocytes differentiated from mouse preadipocytes[32] (**Fig. 6g**) and cocultured them with IL-4-stimulated *Ern1*$^{f/f}$; *Lyz2*-Cre or *Ern1*$^{f/f}$ BMDMs. Coculture with IL-4-treated BMDMs significantly increased the expression of *Ucp1* and beige-adipocyte markers[33], including *Cd137* (official symbol *Tnfrsf9*), *Ear2* and *Tmem26*, in differentiated beige adipocytes (**Fig. 6h**); moreover, IRE1α deficiency robustly enhanced the ability of IL-4-stimulated BMDMs to upregulate these signature genes of beige adipocytes (**Fig. 6h**). Thus, IRE1α abrogation augments M2 polarization of ATMs and consequently enables more efficient WAT browning.

Next, to explore the mechanisms by which IRE1α promotes M2 polarization, we performed global gene expression analysis by RNA-seq on IL-4-stimulated BMDMs. Of the 755 genes significantly upregulated (>1.25-fold, $P < 0.05$ by two-tailed rank product nonparametric method) by IL-4, ~11% were attenuated, and ~10% were further enhanced by IRE1α ablation in *Ern1*$^{f/f}$; *Lyz2*-Cre BMDMs. In contrast, among the 797 genes significantly downregulated (>1.25-fold, $P < 0.05$), ~15% were attenuated, and ~13% were further suppressed (**Supplementary Fig. 6a**). Gene set enrichment analysis (GSEA) showed that IRE1α abrogation resulted in alterations of multiple cellular-function and signaling pathways, including augmented IL-4 stimulation of oxidative phosphorylation, enhanced IL-4 suppression of the Notch pathway, and attenuated cytokine and chemokine signaling (**Supplementary Fig. 6b**). IRE1α ablation resulted in changes in the expression of a diversity of IL-4-regulated potential secretory proteins, including cytokines, chemokines, growth factors and proteins implicated in tissue remodeling (**Supplementary Fig. 6c**). GSEA also revealed enhanced upregulation of most IL-4-induced M2-marker genes as a result of IRE1α deficiency (**Fig. 7a**). Moreover, motif analysis identified a number of regulatory transcription factors involved in IL-4-induced gene expression programs, including the interferon regulatory factor (IRF) and Krüppel-like factor (KLF) family members, which were found to be influenced by IRE1α ablation. Alignment of the expression heat maps indicated that IL-4 upregulated the expression of *Irf1*, *Irf4* and *Klf4*, whose expression was appreciably enhanced in *Ern1*$^{f/f}$; *Lyz2*-Cre cells (**Fig. 7b**). Given that both IRF4 and KLF4 have been shown to be the critical regulators of M2 polarization[34–36], we examined their expression by quantitative RT–PCR. IRE1α ablation, which abolished IL-4-induced changes in *Xbp1* mRNA splicing and the expression of two RIDD-target genes[22], *Pmp22* and *Hgsnat*, significantly augmented IL-4 induction of both *Irf4* and *Klf4* expression in BMDMs (**Fig. 7c**) but exerted no effect on IL-4 upregulation of *Pparg* or *Ppard*, two other key regulators of M2 activation[37,38]. Therefore, the effects of IRE1α deficiency on *Irf4* and *Klf4* expression mirrored the effects on the two RIDD targets examined.

To determine whether IRE1α downregulated the expression of *Irf4* and *Klf4* through a mechanism dependent on its RNase activity, we treated BMDMs with 4μ8C, a pharmacologic inhibitor of IRE1α's RNase activity[39,40]. Although IL-4 stimulated IRE1α phosphorylation (**Fig. 7d**) as well as *Xbp1* mRNA splicing (**Fig. 7e**), treatment with 4μ8C further enhanced IRE1α phosphorylation but effectively blocked *Xbp1* mRNA splicing (**Fig. 7d**,**e**) and increased IL-4 induction of Ym-1 protein expression without affecting STAT6 phosphorylation (**Fig. 7d**). In contrast to its inhibitory effect on IL-4-induced *Xbp1* mRNA splicing, 4μ8C significantly enhanced IL-4 induction of *Pmp22* and *Hgsnat* as well as *Irf4*, *Klf4* and other M2-marker genes (**Fig. 7e**). 4μ8C's augmentative effect on IL-4 upregulation of *Irf4*, *Klf4* and *Chil3* was abolished in *Ern1*$^{f/f}$; *Lyz2*-Cre BMDMs, thus indicating its specific action against IRE1α (**Fig. 7f**). These data suggested that IRE1α downregulates *Irf4* and *Klf4* expression and exerts its suppressive effect on M2 polarization, through a mechanism that requires its RNase activity but presumably not its *Xbp1* mRNA splicing activity. To further confirm the involvement of the XBP1 pathway, we tested the effect of ectopic expression of the spliced, transcriptionally active form, XBP1s.

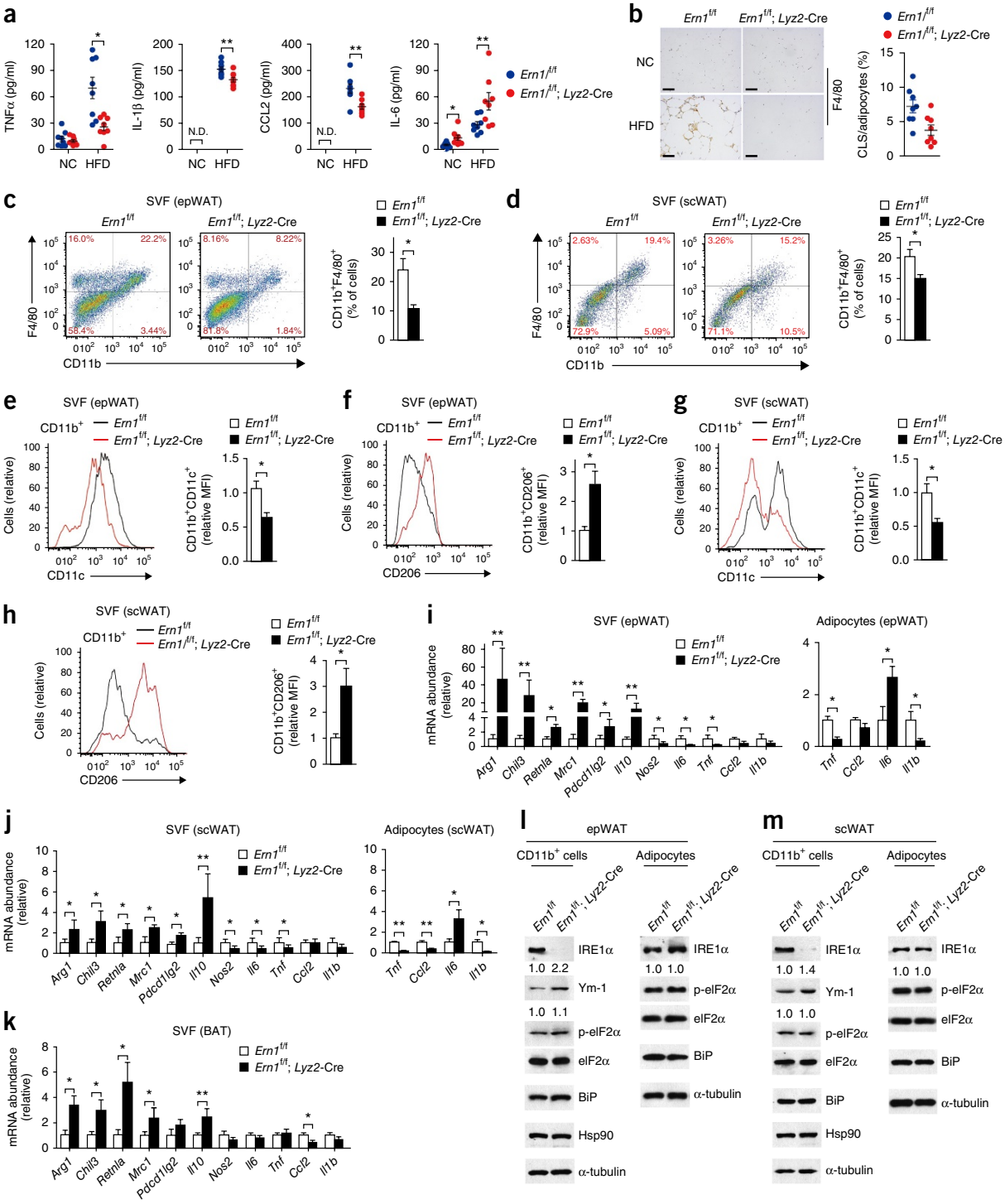

Figure 5 IRE1α deficiency reverses the M1–M2 imbalance of ATMs. (**a**,**b**) *Ern1*$^{f/f}$; *Lyz2*-Cre and *Ern1*$^{f/f}$ mice were fed an NC ($n = 8$ per group) or HFD ($n = 10$ per group) for 16 weeks. (**a**) Serum concentrations of the indicated cytokines. N.D., not detected. (**b**) F4/80 IHC of epWAT sections (5 images per mouse). Scale bars, 200 μm. F4/80$^+$ crown-like structures (CLS) were quantified. (**c**–**m**) *Ern1*$^{f/f}$; *Lyz2*-Cre and *Ern1*$^{f/f}$ mice were fed an HFD for 16 weeks (**c**–**h**, $n = 5$ per group; **i**–**k**, $n = 8$ per group; **l**,**m**, $n = 5$ per group). (**c**,**d**) Representative flow cytometry histograms from analysis of CD11b and F4/80 expression in SVFs of epWAT (**c**) and scWAT (**d**) ($n = 5$ histograms per group). Percentages of CD11b$^+$F4/80$^+$ cells are also shown. (**e**–**h**) Flow cytometry analyses of the expression of CD11c and CD206 from CD11b$^+$ cells in SVFs of epWAT (**e**,**f**) and scWAT (**g**,**h**), respectively. Amounts of CD11b$^+$CD11c$^+$ and CD11b$^+$CD206$^+$ cells are quantified and presented as relative mean fluorescence intensity (MFI). (**i**–**k**) Quantitative RT–PCR analyses of the mRNA abundance of the indicated genes in SVFs and adipocytes from epWAT (**i**) and scWAT (**j**), and in SVFs from BAT (**k**). (**l**,**m**) Immunonblot analyses of Ym-1 and IRE1α protein along with the indicated UPR markers in lysates of CD11b$^+$ cells or adipocytes isolated from epWAT (**l**) and scWAT (**m**). α-tubulin is a loading control. Each lane represents a pooled sample from 5 mice analyzed in duplicate. Numerical values indicate the relative levels of Ym-1 protein and eIF2α phosphorylation (p-eIF2α/eIF2α ratio). Data are shown as mean ± s.e.m., $^*P < 0.05$; $^{**}P < 0.01$ by two-tailed Student's *t* test or two-way ANOVA.

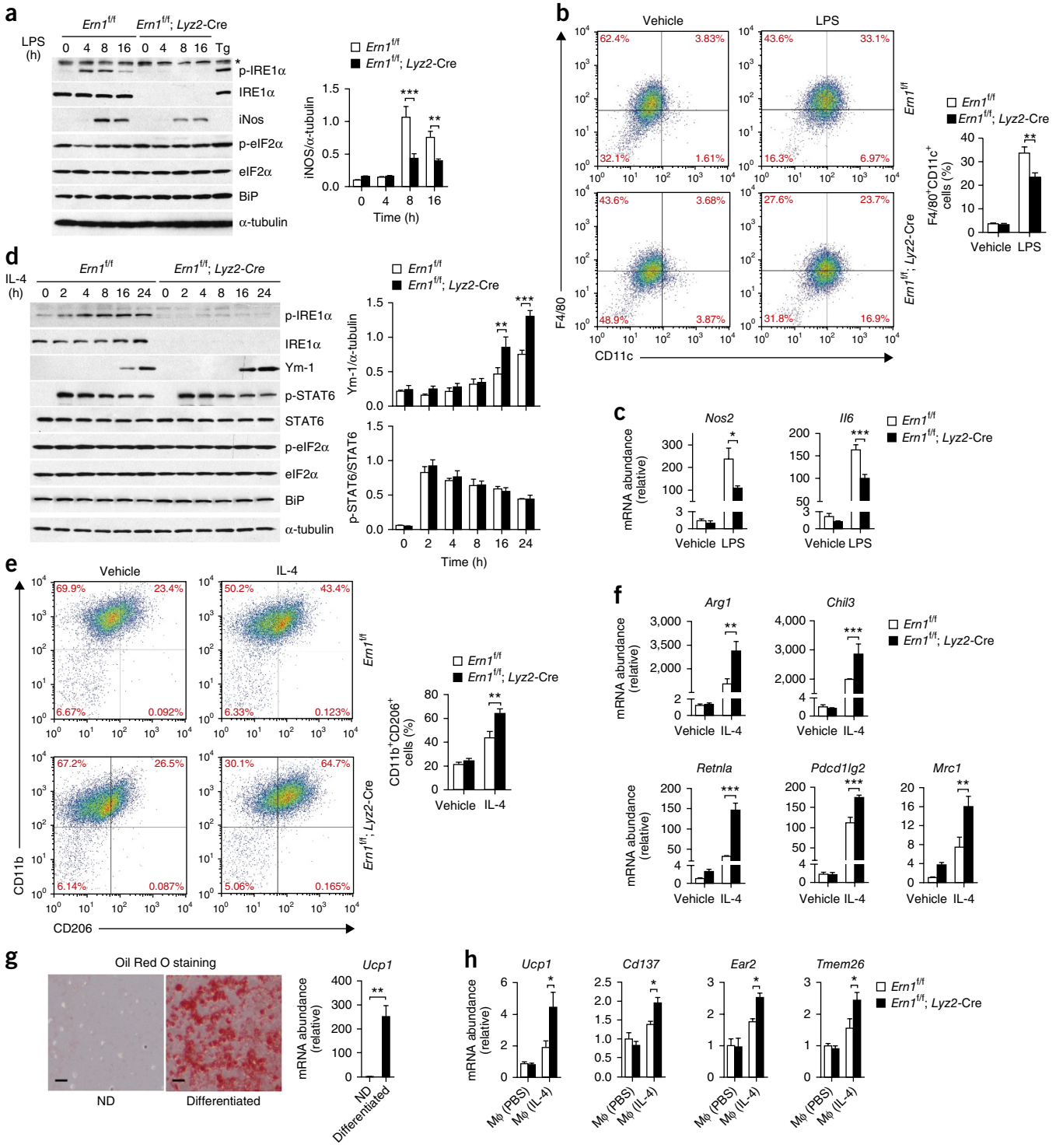

Figure 6 Abrogation of IRE1α promotes M2 but decreases M1 polarization of macrophages. (**a**–**f**) BMDMs from *Ern1*$^{f/f}$; *Lyz2*-Cre mice and *Ern1*$^{f/f}$ littermates were treated with 100 ng/ml LPS (**a**–**c**) or 20 ng/ml IL-4 (**d**–**f**) or vehicle control (3 and 4 independent experiments, respectively). (**a**) Immunoblot analysis of IRE1α and iNOS protein and the indicated UPR markers in cell lysates of LPS-treated BMDMs. Asterisk indicates a nonspecific band. Quantification of iNOS protein is shown. α-tubulin is a loading control. (**b**,**c**) BMDMs were treated with LPS for 24 h. (**b**) Flow cytometry analysis of the expression of F4/80 and CD11c. Percentages of F4/80$^+$CD11c$^+$ cells are shown. (**c**) Relative mRNA abundance of *Nos2* (iNos) and *Il6*. (**d**) Immunoblot analysis of cell lysates of IL-4-stimulated BMDMs. Quantification of Ym-1 protein and phosphorylated STAT6 is shown. (**e**,**f**) BMDMs were treated with IL-4 for 24 h. (**e**) Flow cytometry analysis of the expression of CD11b and CD206, and percentages of CD11b$^+$CD206$^+$ cells are shown. (**f**) Relative mRNA abundance of the indicated M2-marker genes. (**g**,**h**) Stimulation of beige adipocytes by IL-4-treated BMDMs *in vitro*. (**g**) Differentiation of beige adipocytes. Shown are images of cells stained with Oil Red O (Scale bars, 400 μm) and the relative *Ucp1* mRNA abundance in nondifferentiated (ND) preadipocytes versus differentiated beige cells. (**h**) Relative mRNA abundance of *Ucp1* and the indicated beige adipocyte markers in differentiated cells after coculture with PBS- or IL-4-treated BMDMs from *Ern1*$^{f/f}$; *Lyz2*-Cre or *Ern1*$^{f/f}$ mice. Results are presented as mean ± s.e.m., $^*P < 0.05$; $^{**}P < 0.01$; $^{***}P < 0.001$ by two-tailed Student's *t* test or two-way ANOVA.

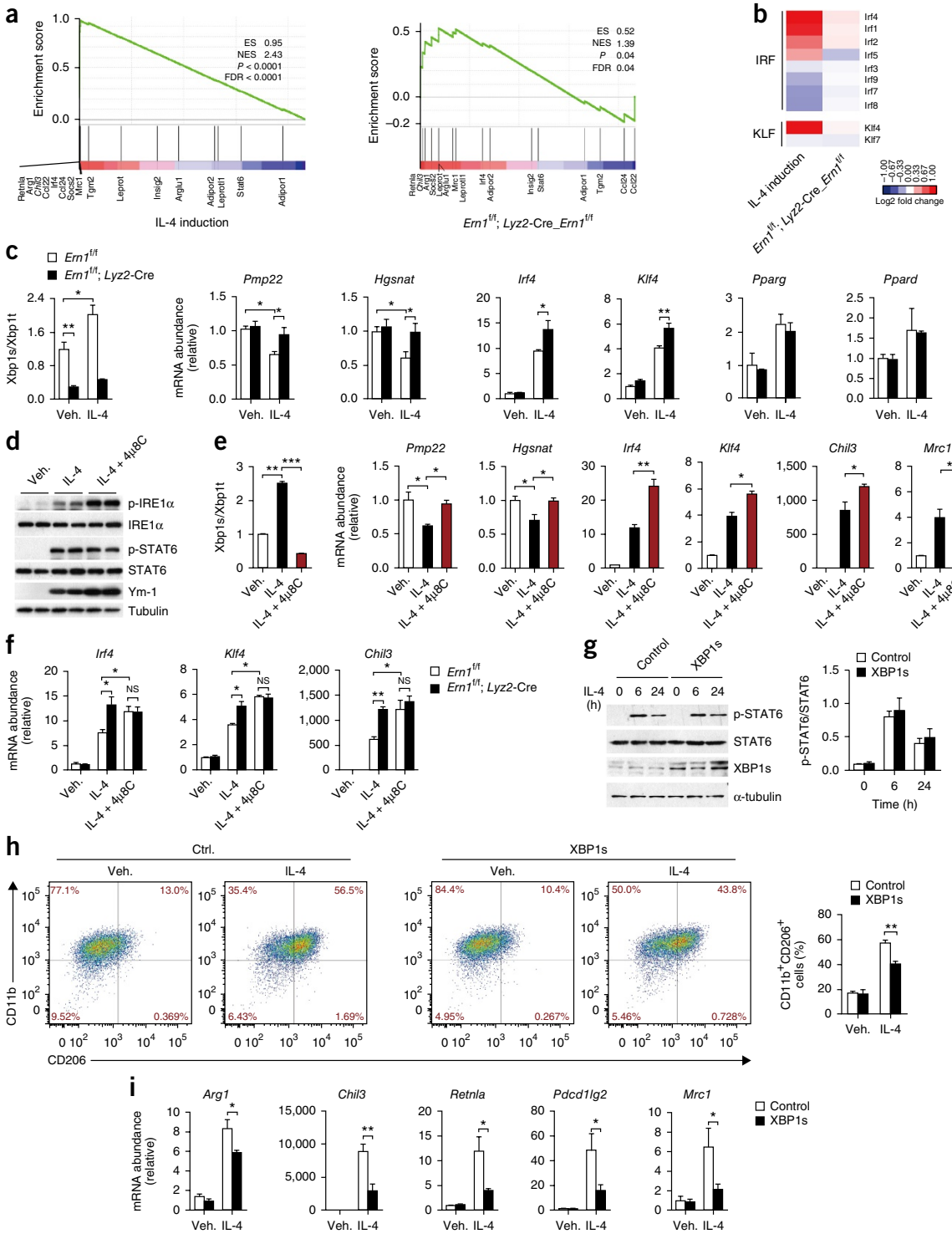

Figure 7 IRE1α augments M2 polarization via an RNase-dependent mechanism. (**a**–**c**) *Ern1*$^{f/f}$; *Lyz2*-Cre and *Ern1*$^{f/f}$ BMDMs were treated with 20 ng/ml IL-4 versus vehicle (veh.) for 24 h. (**a**,**b**) RNA-seq analysis (2 independent experiments). (**a**) Gene set enrichment analysis. Enrichment scores are shown for 16 M2 markers regulated by IL-4 (left) and those affected by IRE1α deficiency under IL-4 stimulation (right). Genes are ranked according to their expression changes induced by IL-4 or resulting from IRE1α deficiency. ES, enrichment score; NES, normalized enrichment score; FDR, false discovery rate. (**b**) Heat maps showing IL-4-induced changes in the expression of the indicated IRF and KLF family members, as aligned with those altered in *Ern1*$^{f/f}$; *Lyz2*-Cre relative to *Ern1*$^{f/f}$ cells under IL-4 stimulation. (**c**) *Xbp1* mRNA splicing and the mRNA abundance of the indicated genes. (**d**,**e**) Mouse BMDMs were treated with vehicle, IL-4 or IL-4 plus 4μ8C at 1 μM for 24 h. (**d**) Immunoblot analysis of IRE1α and STAT6 phosphorylation and Ym-1 protein. (**e**) *Xbp1* mRNA splicing and the mRNA abundance of the indicated genes. (**f**) *Ern1*$^{f/f}$; *Lyz2*-Cre and *Ern1*$^{f/f}$ BMDMs were stimulated with IL-4 in the absence or presence of 4μ8C. Relative mRNA abundance of *Irf4*, *Klf4* and *Chil3*. (**g**–**i**) BMDMs were infected by control or XBP1s-expressing lentiviruses and then treated with IL-4. (**g**) Immunoblot analysis and quantification of STAT6 phosphorylation. (**h**,**i**) Infected BMDMs were treated with IL-4 for 24 h. (**h**) Flow cytometry. Percentages of CD11b^{+}CD206^{+} cells. (**i**) Relative mRNA abundance of the indicated genes. Results are mean ± s.e.m. from 3 (**c**–**g**) or 4 (**h**–**i**) independent experiments. **P* < 0.05; ***P* < 0.01; ****P* < 0.001; NS, not significant by one-way or two-way ANOVA.

Lentiviral overexpression of XBP1s in BMDMs did not affect IL-4 stimulation of STAT6 phosphorylation (**Fig. 7g**) or IL-4 induction of *Irf4* or *Klf4* (**Supplementary Fig. 7a**,**b**). However, flow cytometry of IL-4-stimulated, XBP1s-overexpressing BMDMs showed a significant decrease (by ~29%) in $CD11b^{+}CD206^{+}$ M2-like cells (**Fig. 7h**), along with robust decreases in IL-4 induction of signature M2 markers (**Fig. 7i**). Thus, XBP1s also contributes to IRE1α-mediated suppression of M2 polarization; however, whether this effect is achieved through its transcriptional activity or other actions remains to be determined. These results suggest that the IRE1α pathways, which are activated by IL-4 in macrophages, may constitute a negative feedback loop suppressing M2 polarization.

DISCUSSION

ER stress is thought to underlie the pathogenic progression of obesity, insulin resistance and type 2 diabetes[41,42], but the precise physiological mechanisms connecting ER stress to metabolic dysfunctions are poorly understood. Here, our studies uncovered a key role of the macrophage IRE1α pathway in mediating metabolic ER stress-induced malfunction in both brown and beige fat, symptoms increasingly being recognized as a hallmark of the pathogenic development of obesity and metabolic syndrome[4,24]. Our findings offer a new paradigm with respect to how metabolic ER stress disrupts glucose and energy metabolism: during overnutrition, obesogenic factors (for example, fatty acids and LPS) activate macrophage IRE1α, thus defining an intracellular context repressing M2 while enhancing M1 polarization; such an M1–M2 imbalance of ATMs in turn severely limits the energy utilization capacity of both brown and beige fat in addition to promoting insulin resistance.

Our results demonstrated that abrogation of myeloid IRE1α in mice results in a broad range of metabolically beneficial effects, particularly robust augmentation of the thermogenic activity of both brown and beige fat. These metabolic phenotypes are largely ascribable to the functional changes in ATMs, i.e., the enhanced M2 activation of resident macrophages in both BAT and scWAT, which have been reported to secrete catecholamines that drive adaptive thermogenesis[13,14]. Indeed, we detected higher tissue content of norepinephrine in both BAT and scWAT from *Ern1*$^{f/f}$; *Lyz2*-Cre mice; however, we cannot exclude the possibility that macrophage IRE1α deficiency might directly affect the biosynthesis and/or secretion of catecholamines within ATMs or indirectly influence catecholamine release by local neurons in adipose tissue. In addition, other macrophage-derived factors affected by IRE1α ablation may also mediate the intercellular cross-talk between ATMs and adipocytes[43], thereby leading to more robust activation of brown and beige fat. For instance, it remains to be defined which IRE1α-regulated secretory factors from M2-polarized ATMs may modulate the differentiation and thermogenic activation of beige adipocytes. Moreover, the augmentation of BAT activity and WAT browning as a result of the correction of the M1–M2 imbalance of ATMs in *Ern1*$^{f/f}$; *Lyz2*-Cre mice might directly contribute to improvements in insulin sensitivity and systemic glucose homeostasis in a manner independent of fat utilization[23]. With regard to the mechanisms by which IRE1α controls the shift in the M1–M2 polarization programs, it is likely that multiple regulatory modes exist, namely through IRE1α's RIDD activity as well as XBP1s-dependent actions.

Notably, IRE1α was also partially ablated in neutrophils of *Ern1*$^{f/f}$; *Lyz2*-Cre mice. Although the contribution of neutrophil IRE1α during adipose inflammation has yet to be clarified, our results clearly demonstrated that specific depletion of ATMs abolished the augmentative effects of myeloid IRE1α deficiency on the browning of scWAT. This finding strongly suggests that IRE1α ablation in macrophages, rather than in neutrophils, should account for most of the observed enhancement in energy expenditure and metabolic improvements. This possibility is consistent with findings from a report showing that changes in adipose neutrophils have no effect on adiposity after HFD feeding[44]. We also observed an unusual elevation of circulating IL-6, along with higher *Il6* expression in white adipocytes of *Ern1*$^{f/f}$; *Lyz2*-Cre mice. Given its demonstrated roles in activating brown and beige fat and in promoting M2 polarization of ATMs[45,46], IL-6 may also be an important contributor to augmenting adaptive thermogenesis via a feed-forward loop, thereby further enhancing M2 activation of ATMs in *Ern1*$^{f/f}$; *Lyz2*-Cre mice. Currently, how IRE1α-deficient ATMs communicate with adipocytes in increasing *Il6* expression, while decreasing that of other proinflammatory cytokines, remains enigmatic.

In short, our findings revealed that the macrophage IRE1α pathway is a crucial driver in metabolic ER stress and the promotion of energy imbalance and obesity. Blocking IRE1α causes profound alterations in the functional activities of macrophages, which may range beyond the shifting of oversimplified M1–M2 polarization states[27]. Nonetheless, targeted modulation of IRE1α activity in ATMs might open new avenues for developing brown- and beige-fat-enhancing therapeutics to treat obesity and metabolic disease.

METHODS

Methods, including statements of data availability and any associated accession codes and references, are available in the online version of the paper.

Note: Any Supplementary Information and Source Data files are available in the online version of the paper.

ACKNOWLEDGMENTS

We thank S. Kajimura from UCSF for the beige preadipocytes and C. Jiang from Peking University for assistance with the macrophage depletion experiments. This work was supported by grants from the Ministry of Science and Technology (2016YFA0500100 and 973 Program 2012CB524900) and the National Natural Science Foundation of China (81420108006, 31690102 and 31230036) to Y.L.; the National Natural Science Foundation of China (31671181 and 31371153) to S.Z.D.; the National Natural Science Foundation of China (91539107) to Jianmiao Liu; and the National Natural Science Foundation of China (31671227 and 91642113) to Y.Q. This work was also supported by a research grant from the European Foundation for the Study of Diabetes/Chinese Diabetes Society/Lilly Programme to Y.L.

AUTHOR CONTRIBUTIONS

B. Shan, S.-Z.D. and Y.L. conceived and designed the studies. B. Shan, X.W. and Y.W. performed most of the experiments and analyzed the data. C.X. and J.-D.J.H. conducted the bioinformatics analysis. Z.X., J.D., M.S., S.H., F.Z., L.Y. and M.Z. performed some of the animal and cell experiments. F.N., J. Li, Jianmiao Liu, Jianfeng Liu, Y.Q., W.J., B. Song, S.-Z.D. and L.R. provided essential reagents and assisted with experimental design and data analysis. B. Shan and Y.L. wrote the manuscript.

COMPETING FINANCIAL INTERESTS

The authors declare no competing financial interests.

1. Lumeng, C.N., Bodzin, J.L. & Saltiel, A.R. Obesity induces a phenotypic switch in adipose tissue macrophage polarization. *J. Clin. Invest.* **117**, 175–184 (2007).
2. Hotamisligil, G.S. Endoplasmic reticulum stress and the inflammatory basis of metabolic disease. *Cell* **140**, 900–917 (2010).
3. Lumeng, C.N. & Saltiel, A.R. Inflammatory links between obesity and metabolic disease. *J. Clin. Invest.* **121**, 2111–2117 (2011).
4. Rosen, E.D. & Spiegelman, B.M. What we talk about when we talk about fat. *Cell* **156**, 20–44 (2014).
5. Brestoff, J.R. & Artis, D. Immune regulation of metabolic homeostasis in health and disease. *Cell* **161**, 146–160 (2015).

6. Biswas, S.K. & Mantovani, A. Orchestration of metabolism by macrophages. *Cell Metab.* **15**, 432–437 (2012).
7. Odegaard, J.I. & Chawla, A. Alternative macrophage activation and metabolism. *Annu. Rev. Pathol.* **6**, 275–297 (2011).
8. Osborn, O. & Olefsky, J.M. The cellular and signaling networks linking the immune system and metabolism in disease. *Nat. Med.* **18**, 363–374 (2012).
9. McNelis, J.C. & Olefsky, J.M. Macrophages, immunity, and metabolic disease. *Immunity* **41**, 36–48 (2014).
10. Chawla, A., Nguyen, K.D. & Goh, Y.P. Macrophage-mediated inflammation in metabolic disease. *Nat. Rev. Immunol.* **11**, 738–749 (2011).
11. Odegaard, J.I. & Chawla, A. The immune system as a sensor of the metabolic state. *Immunity* **38**, 644–654 (2013).
12. Gordon, S. Alternative activation of macrophages. *Nat. Rev. Immunol.* **3**, 23–35 (2003).
13. Nguyen, K.D. *et al.* Alternatively activated macrophages produce catecholamines to sustain adaptive thermogenesis. *Nature* **480**, 104–108 (2011).
14. Qiu, Y. *et al.* Eosinophils and type 2 cytokine signaling in macrophages orchestrate development of functional beige fat. *Cell* **157**, 1292–1308 (2014).
15. Rao, R.R. *et al.* Meteorin-like is a hormone that regulates immune-adipose interactions to increase beige fat thermogenesis. *Cell* **157**, 1279–1291 (2014).
16. Ron, D. & Walter, P. Signal integration in the endoplasmic reticulum unfolded protein response. *Nat. Rev. Mol. Cell Biol.* **8**, 519–529 (2007).
17. Walter, P. & Ron, D. The unfolded protein response: from stress pathway to homeostatic regulation. *Science* **334**, 1081–1086 (2011).
18. Hetz, C. The unfolded protein response: controlling cell fate decisions under ER stress and beyond. *Nat. Rev. Mol. Cell Biol.* **13**, 89–102 (2012).
19. Hetz, C., Martinon, F., Rodriguez, D. & Glimcher, L.H. The unfolded protein response: integrating stress signals through the stress sensor IRE1alpha. *Physiol. Rev.* **91**, 1219–1243 (2011).
20. Boden, G. *et al.* Increase in endoplasmic reticulum stress-related proteins and genes in adipose tissue of obese, insulin-resistant individuals. *Diabetes* **57**, 2438–2444 (2008).
21. Gregor, M.F. *et al.* Endoplasmic reticulum stress is reduced in tissues of obese subjects after weight loss. *Diabetes* **58**, 693–700 (2009).
22. Maurel, M., Chevet, E., Tavernier, J. & Gerlo, S. Getting RIDD of RNA: IRE1 in cell fate regulation. *Trends Biochem. Sci.* **39**, 245–254 (2014).
23. Shao, M. *et al.* Hepatic IRE1alpha regulates fasting-induced metabolic adaptive programs through the XBP1s-PPARα axis signalling. *Nat. Commun.* **5**, 3528 (2014).
24. Kajimura, S., Spiegelman, B.M. & Seale, P. Brown and beige fat: physiological roles beyond heat generation. *Cell Metab.* **22**, 546–559 (2015).
25. Jordan, M.B., van Rooijen, N., Izui, S., Kappler, J. & Marrack, P. Liposomal clodronate as a novel agent for treating autoimmune hemolytic anemia in a mouse model. *Blood* **101**, 594–601 (2003).
26. Feng, B. *et al.* Clodronate liposomes improve metabolic profile and reduce visceral adipose macrophage content in diet-induced obese mice. *PLoS One* **6**, e24358 (2011).
27. Murray, P.J. *et al.* Macrophage activation and polarization: nomenclature and experimental guidelines. *Immunity* **41**, 14–20 (2014).
28. Mao, T. *et al.* PKA phosphorylation couples hepatic inositol-requiring enzyme 1alpha to glucagon signaling in glucose metabolism. *Proc. Natl. Acad. Sci. USA* **108**, 15852–15857 (2011).
29. Wang, X.X. *et al.* Isolation of high quality RNA and construction of a suppression subtractive hybridization library from ramie (*Boehmeria nivea* L. Gaud.). *Mol. Biol. Rep.* **37**, 2099–2103 (2010).
30. Martinon, F., Chen, X., Lee, A.H. & Glimcher, L.H. TLR activation of the transcription factor XBP1 regulates innate immune responses in macrophages. *Nat. Immunol.* **11**, 411–418 (2010).
31. Kim, S. *et al.* Endoplasmic reticulum stress-induced IRE1alpha activation mediates cross-talk of GSK-3beta and XBP-1 to regulate inflammatory cytokine production. *J. Immunol.* **194**, 4498–4506 (2015).
32. Shinoda, K. *et al.* Genetic and functional characterization of clonally derived adult human brown adipocytes. *Nat. Med.* **21**, 389–394 (2015).
33. Wu, J. *et al.* Beige adipocytes are a distinct type of thermogenic fat cell in mouse and human. *Cell* **150**, 366–376 (2012).
34. Satoh, T. *et al.* The Jmjd3-Irf4 axis regulates M2 macrophage polarization and host responses against helminth infection. *Nat. Immunol.* **11**, 936–944 (2010).
35. Eguchi, J. *et al.* Interferon regulatory factor 4 regulates obesity-induced inflammation through regulation of adipose tissue macrophage polarization. *Diabetes* **62**, 3394–3403 (2013).
36. Liao, X. *et al.* Kruppel-like factor 4 regulates macrophage polarization. *J. Clin. Invest.* **121**, 2736–2749 (2011).
37. Odegaard, J.I. *et al.* Macrophage-specific PPARγ controls alternative activation and improves insulin resistance. *Nature* **447**, 1116–1120 (2007).
38. Kang, K. *et al.* Adipocyte-derived Th2 cytokines and myeloid PPARdelta regulate macrophage polarization and insulin sensitivity. *Cell Metab.* **7**, 485–495 (2008).
39. Volkmann, K. *et al.* Potent and selective inhibitors of the inositol-requiring enzyme 1 endoribonuclease. *J. Biol. Chem.* **286**, 12743–12755 (2011).
40. Cross, B.C. *et al.* The molecular basis for selective inhibition of unconventional mRNA splicing by an IRE1-binding small molecule. *Proc. Natl. Acad. Sci. USA* **109**, E869–E878 (2012).
41. Wang, M. & Kaufman, R.J. Protein misfolding in the endoplasmic reticulum as a conduit to human disease. *Nature* **529**, 326–335 (2016).
42. Ozcan, U. *et al.* Endoplasmic reticulum stress links obesity, insulin action, and type 2 diabetes. *Science* **306**, 457–461 (2004).
43. Hui, X. *et al.* Adiponectin enhances cold-induced browning of subcutaneous adipose tissue via promoting M2 macrophage proliferation. *Cell Metab.* **22**, 279–290 (2015).
44. Talukdar, S. *et al.* Neutrophils mediate insulin resistance in mice fed a high-fat diet through secreted elastase. *Nat. Med.* **18**, 1407–1412 (2012).
45. Petruzzelli, M. *et al.* A switch from white to brown fat increases energy expenditure in cancer-associated cachexia. *Cell Metab.* **20**, 433–447 (2014).
46. Mauer, J. *et al.* Signaling by IL-6 promotes alternative activation of macrophages to limit endotoxemia and obesity-associated resistance to insulin. *Nat. Immunol.* **15**, 423–430 (2014).

ONLINE METHODS

Animals. All experimental protocols were approved by the Institutional Animal Care and Use Committee at the Institute for Nutritional Sciences, Shanghai Institutes for Biological Sciences, Chinese Academy of Sciences. C57BL/6J mice were purchased from Shanghai Laboratory Animal Co. Ltd. To generate myeloid-specific IRE1α-knockout *Ern1*$^{f/f}$ mice, in which exon 2 of the *Ern1* allele was flanked by *lox*P sites, were created and backcrossed into the C57BL/6J genetic background as previously described[23]. *Ern1*$^{f/f}$; *Lyz2*-Cre mice were subsequently produced via intercrossing *Ern1*$^{f/f}$ mice with *Lyz2*-Cre (i.e., LysM-Cre) mice, which express the Cre recombinase transgene under the control of the lysozyme 2 gene promoter/enhancer elements[13]. Animals were housed in laboratory cages at 23 ± 3 °C unless specifically indicated, with a humidity of 35 ± 5% under a 12-h dark/light cycle (lights on at 6:30 a.m.). Mice were maintained on a normal chow (NC) diet (Shanghai Laboratory Animal Co. Ltd). For diet-induced obesity, male *Ern1*$^{f/f}$ mice and their *Ern1*$^{f/f}$; *Lyz2*-Cre littermates were fed a high-fat diet (HFD, 60% kcal fat; Research Diets) for 16 weeks, starting at 8 weeks of age. For cold-exposure experiments, single-housed male mice at 10 weeks of age were placed in prechilled cages and exposed to a cold environment (4 °C) for the desired time periods. For controls at room temperature (RT), mice were placed in a laboratory incubator at 25 °C. To deplete macrophages in subcutaneous white adipose tissue (scWAT), clodronate-liposomes (F70101C, Neutrol, FormuMax) or control liposomes were subcutaneously injected into the scWAT of 10-week-old male *Ern1*$^{f/f}$ and *Ern1*$^{f/f}$; *Lyz2*-Cre mice. For each animal, 100 µl clodronate liposomes was administered once daily for 4 d into scWAT on one side, and 100 µl control liposomes was administered on the other side. Mice were then exposed to cold at 4 °C for 72 h. No statistical method was used to predetermine sample size. The experiments were not randomized and were not performed with blinding.

Metabolic phenotyping. Whole-body fat and lean mass was measured by ^{1}H-nuclear magnetic resonance (NMR) spectroscopy. To analyze energy expenditure, single-housed mice were acclimated for 24 h to an OxyMax Comprehensive Laboratory Animal Monitoring System (CLAMS, Columbus Instruments) before oxygen consumption and physical activity were monitored for 24 h. Oxygen consumption (VO_2) was calculated after normalization to lean mass. For glucose tolerance tests (GTT), mice were fasted for 16 h before intraperitoneal injection of glucose at 1 g/kg body weight. For insulin tolerance tests (ITT), mice fasted for 4 h were injected with insulin (Roche) at 0.75 U/kg body weight. Blood glucose was determined with a glucometer (FreeStyle) before injection (0 min) or at 15, 30, 60 or 90 min after injection. Serum levels of triglycerides (TGs), cholesterol, free fatty acids (FFAs), insulin, leptin, adiponectin, IL-6, IL-1β, CCL2, TNF and norepinephrine were measured with a serum triglyceride determination kit (Sigma, Triglyceride Reagent T2449 and Free Glycerol Reagent F6428), FFA assay kit (Cayman Chemical, 700310), insulin ELISA kit (Millipore, EZRMI-13K), leptin ELISA kit (ADI-900-019A, ENZO), adiponectin ELISA kit (KMP0041, ThermoFisher), IL-6 ELISA kit (ADI-900-045, ENZO), IL-1β ELISA kit (ADI-900-132A, ENZO), CCL2 ELISA kit (ADI-900-077, ENZO), TNF ELISA kit (ADI-900-047, ENZO) and norepinephrine ELISA kit (BA E-5200, Rocky Mountain Diagnostics), respectively, according to the manufacturers' instructions. Hepatic TGs were analyzed as previously described[23]. Briefly, 40–50 mg of liver tissue was homogenized in PBS and mixed with $CHCl_3$/CH_3OH (2:1 (vol/vol). The organic phase was transferred, air-dried overnight and resuspended in 1% Triton X-100 in absolute ethanol. The concentration of TGs was likewise determined with a serum triglyceride determination kit (Sigma).

Histologic analysis and immunohistochemistry. Adipose tissues or livers were fixed in 10% neutral formalin for at least 48 h at 4 °C and then desiccated and embedded in paraffin before being cut into 5-µm sections and stained with hematoxylin and eosin (H&E) or analyzed by immunohistochemistry (IHC). For IHC, adipose tissue sections were rehydrated and then boiled in 10 mM citric acid buffer, pH 6.0, at 95 °C for antigen retrieval, and endogenous peroxidases were quenched with 3% hydrogen peroxide. After incubation with anti-UCP1 (ab10983, Abcam) or anti-F4/80 (MCA497, AbDSerotec), a biotinylated secondary antibody (PV6004, ZSGB-BIO) was used before development according to the manufacturer's instructions for the DAB Staining Kit (PV6000, ZSGB-BIO). Validation information is available on the manufacturers' websites. After being counterstained in hematoxylin, sections were dehydrated for mounting. Microscopy analysis was done with an Olympus BX61 microscope.

Isolation of stromal vascular fractions and macrophages from WAT. The SVFs and adipocytes were prepared as previously described[1] with minor modifications. Mouse epWAT or scWAT and BAT were isolated and digested with 0.1% collagenase type I (Sigma-Aldrich) at 37 °C with shaking at 200 r.p.m. for 60–90 min. Digested tissues were filtered through a 70-µM nylon mesh and centrifuged at 500*g* for 5 min. Floating adipocytes and SVF pellets were collected, and the SVFs were resuspended in red-blood-cell lysis buffer (eBioscience RBC Lysis Buffer) before further analysis. To isolate ATMs, SVFs were washed with PBS and incubated with CD11b (Microglia) MicroBeads (130-093-634, MiltenyiBiotec) for 1 h, then subjected to magnetic separation with an LS column (130-042-410, MiltenyiBiotec).

Flow cytometry. Recovered SVFs or magnetically isolated CD11b$^+$ cells were washed and incubated with the desired combination of fluorochrome-conjugated antibodies, including PE-Cy7-anti-CD11b (clone M1/70, eBioscience), FITC-anti-F4/80 (clone BM8, eBioscience), APC-anti-CD11c (clone N418, eBioscience), PE-anti-CD206 (clone MR5D3, AbDSerotec), PE-Cy7-anti-CD45 (clone 30-F11, eBioscience), APC-anti-CD11b (clone M1/70, eBioscience), PE-anti-F4/80 (clone EM8, eBioscience) and anti-Ly6G (clone RB6-8C5, eBioscience). Validation information is available on the manufacturers' websites. Cells were then subjected to flow cytometry analysis with a BD FACSAria IIu flow cytometer (BD Bioscience). Data were analyzed with FlowJo Software version 7.6.4.

Isolation of spleen immune cells and peritoneal macrophages. For analysis of IRE1α ablation in immune cells, CD4$^+$ T cells, B cells and neutrophils were isolated from the spleens of *Ern1*$^{f/f}$ mice and their *Ern1*$^{f/f}$; *Lyz2*-Cre littermates. Briefly, spleens were crushed and filtered with a strainer to obtain single-cell suspensions. CD4$^+$ T cells were enriched with magnetic CD4 (L3T4) MicroBeads (130-049-201, MiltenyiBiotec), according to the manufacturer's instructions. B cells and neutrophils were sorted by flow cytometry with FITC-anti-B220 (clone RA3-6B2, eBioscience) and anti-Ly6G (clone RB6-8C5, eBioscience), respectively. Peritoneal macrophages were isolated from mice at 3 d after intraperitoneal injection of thioglycollate broth (70157, Sigma). Isolated cells were then lysed for mRNA preparation before RT–PCR analysis of the region spanning the targeted exon 2 within the *Ern1* mRNA. The oligonucleotide primers with the sequences sense (exon 1) 5′-TCCGTGTCCACCGATCCTCC-3′ and antisense (exon 3) 5′-GCCTTCGTTGTTCTTGCCTC-3′ produced the expected 402-bp PCR product from *Ern1*$^{f/f}$ cells, and a 281-bp PCR product from *Ern1*$^{f/f}$; *Lyz2*-Cre cells, when the 121-bp exon 2 was successfully deleted.

Macrophage polarization assay. BMDMs were prepared as previously described[13]. Briefly, bone-marrow cells were isolated from the femurs and tibias of male C57BL/6J mice or age-matched *Ern1*$^{f/f}$ and *Ern1*$^{f/f}$; *Lyz2*-Cre mice. Cells were maintained in L929-cell-derived differentiation medium for 7 d and allowed to differentiate into mature macrophages. Polarization of BMDMs was induced for M1 activation by treatment with LPS (100 ng/ml, Sigma) or M2 activation with IL-4 (20 ng/ml, Peprotech) for 24 h or the desired time periods before further biochemical or flow cytometry analysis.

Differentiation of beige adipocytes and coculture with BMDMs. Mouse beige preadipocytes (a generous gift from S. Kajimura), generated from the primary SVFs of the inguinal WAT of B6 male mice as previously described[32], were induced to differentiate into beige adipocytes. Briefly, preadipocytes were cultured in growth medium (DMEM supplemented with 10% FBS) and passaged before reaching confluence. When grown to 90% confluency, cells were cultured in the induction medium (growth medium containing 0.5 µg/ml insulin, 1 nM T3, 5 µM dexamethasone, 0.5 mM isobutylmethylxanthine, 1 µM rosiglitazone and 0.125 nM indomethacin). After 36 h, cells were switched to maintenance medium (growth medium with 5 µg/ml insulin and 1 nM T3) and cultured for 6 d, at which point *Ucp1* expression could be detected.

doi:10.1038/ni.3709

For coculturing with mature BMDMs that had been stimulated with PBS or 20 ng/ml IL-4 for 24 h, differentiated beige adipocytes in the lower compartments of Transwell plates (3472, Corning) were incubated for another 24 h with BMDMs in the upper compartments (5×10^4 cells/well). Beige adipocytes were then collected for gene expression analysis.

RNA sequencing (RNA-seq) and bioinformatics analysis. Total cellular RNAs of BMDMs M2-polarized by IL-4 treatment were isolated and subjected to commercial RNA-seq analysis (Berry Genomics). RNA-seq data were uniquely mapped to the mm10 reference genome with TopHat v1.4.1 (ref. 47). Expression values were assigned at the gene level with Cufflinks v1.3.0 (ref. 48). Differentially expressed genes were identified with the R package RankProd[49] on the basis of *P* value <0.01. Hierarchical clustering of gene fold changes was generated in Cluster 3.0 (http://bonsai.hgc.jp/~mdehoon/software/cluster/software.htm) and visualized with JavaTree View. Heat maps were generated to show the average fold changes in gene expression from two independent RNA-seq results, and the Pearson correlation coefficient (PCC) value was calculated between the fold changes shown in two heat maps. Gene set enrichment analysis (GSEA) was performed with the GSEA package (http://software.broadinstitute.org/gsea/index.jsp), and ranked lists of gene fold changes were compared against pathway terms from the KEGG database (http://www.genome.jp/kegg/), with a nominal *P* value <0.05 and a false discovery rate (FDR) <0.25. Motif analysis was conducted with Homer (http://homer.ucsd.edu/homer/) to identify regulatory genes whose binding motifs were present in regions around transcription start sites (−3 kb to +1 kb) of differentially expressed genes. Genes encoding potential secretory proteins were analyzed on the basis of the Gene Ontology database.

Pharmacologic inhibition assay. For pharmacologic inhibition of IRE1α RNase activity, 4μ8C was synthesized in house at the Shanghai Institute of Materia Medica, Chinese Academy of Sciences. BMDMs were treated with IL-4 (Peprotech) at 20 ng/ml for 24 h with or without 4μ8C at 1 μM. Cells were then used for further biochemical analyses.

Lentiviral overexpression of XBP1s in BMDMs. Mouse BMDMs (1×10^6 to 2×10^6 cells) were prepared and infected at a multiplicity of infection (MOI) of 10 with control or XBP1s-overexpressing lentiviruses (Shanghai GeneChem) for 24 h at 37 °C in the presence of 4 mg/ml polybrene. BMDMs were then washed and cultured in fresh medium for 24 h before IL-4 stimulation for further analysis.

Immunoblot analysis and antibodies. Lysates of cells or tissues were prepared with RIPA buffer (150 mM NaCl, 1% NP-40, 0.5% sodium deoxycholate, 0.1% SDS and 50 mM Tris-HCl, pH 7.4) containing complete protease-inhibitor cocktail (Sigma). Proteins separated by SDS–PAGE were transferred onto a polyvinylidene difluoride (PVDF) membrane filter (Millipore). After incubation with the desired antibodies, blots were developed with SuperSignal West Pico Chemiluminescent substrate (Thermo Scientific) or Immunobilon Western Chemiluminescent HRP substrate (Millipore). Protein levels were quantified with NIH ImageJ software. The antibody against phosphorylated IRE1α at Ser724 (p-IRE1α) (NB100-2323) was purchased from Novus Biologicals. Antibodies to UCP1 (ab10983), Ym-1 (ab192029) and Hsp90 (ab13492) were from Abcam. Antibodies to IRE1α (3294), p-Akt (9271), Akt (9272), STAT3 (9139), p-STAT3 (9145), STAT6 (9362), p-STAT6 (9361), eIF2α (5324), p-eIF2α (3398), BiP (3177) and iNOS (13120) were from Cell Signaling. Anti-TH (TA303716) was from OriGene, anti-XBP1 (647501) was from BioLegend, and anti-α-tubulin (T6199) was from Sigma. Validation information is available on the manufacturers' websites.

For phos-tag gel analysis, a 6% SDS–PAGE gel with 25 mM phos-tag was prepared as previously described[50] according to the manufacturer's instructions (Phos-tag acrylamide AAL-107, Wako Pure Chemical Industries). Cell lysates were run at 100 V for 3 h, and separated proteins were transferred onto an NC membrane at 350 mA for 3 h. Anti-IRE1α (3294, Cell Signaling Technology) was used to detect the phosphorylated and nonphosphorylated forms of the IRE1α protein.

Quantitative RT–PCR. Total RNA was isolated with TRIzol reagent (Invitrogen) from cells or tissues. cDNA was synthesized with M-MLV reverse transcriptase and random hexamer primers (Invitrogen). Real-time quantitative PCR was performed with SYBR Green PCR reagents (Applied Biosystems) on an ABI Stepone Plus system (Applied Biosystems). 18s rRNA was used as an internal control for normalization. Oligonucleotide primer pairs used are listed in **Supplementary Table 1**.

Statistical analysis. All data are presented as mean ± s.e.m. Statistical analysis was performed with unpaired two-tailed Student's *t* test, or one-way or two-way analysis of variance (ANOVA) followed by Bonferroni's post test, in GraphPad Prism 5.0. *P* <0.05 was considered to be statistically significant.

Data availability. The RNA-seq data have been deposited in the Gene Expression Omnibus database under accession code GSE94659. The data that support the findings of this study are available from the corresponding author upon request.

47. Trapnell, C., Pachter, L. & Salzberg, S.L. TopHat: discovering splice junctions with RNA-Seq. *Bioinformatics* **25**, 1105–1111 (2009).
48. Trapnell, C. *et al.* Differential gene and transcript expression analysis of RNA-seq experiments with TopHat and Cufflinks. *Nat. Protoc.* **7**, 562–578 (2012).
49. Hong, F. *et al.* RankProd: a bioconductor package for detecting differentially expressed genes in meta-analysis. *Bioinformatics* **22**, 2825–2827 (2006).
50. Yang, L. *et al.* A Phos-tag-based approach reveals the extent of physiological endoplasmic reticulum stress. *PLoS One* **5**, e11621 (2010).